nature materials

ARTICLES

https://doi.org/10.1038/s41563-020-00827-x

Direct X-ray and electron-beam lithography of halogenated zeolitic imidazolate frameworks

Min Tu[1], Benzheng Xia[1], Dmitry E. Kravchenko[1], Max Lutz Tietze[1], Alexander John Cruz[1,2], Ivo Stassen[1], Tom Hauffman[2], Joan Teyssandier[3], Steven De Feyter[3], Zheng Wang[4], Roland A. Fischer[4], Benedetta Marmiroli[5], Heinz Amenitsch[5], Ana Torvisco[5], Miriam de J. Velásquez-Hernández[6], Paolo Falcaro[6,7] and Rob Ameloot[1]✉

Metal–organic frameworks (MOFs) offer disruptive potential in micro- and optoelectronics because of the unique properties of these microporous materials. Nanoscale patterning is a fundamental step in the implementation of MOFs in miniaturized solid-state devices. Conventional MOF patterning methods suffer from low resolution and poorly defined pattern edges. Here, we demonstrate the resist-free, direct X-ray and electron-beam lithography of MOFs. This process avoids etching damage and contamination and leaves the porosity and crystallinity of the patterned MOFs intact. The resulting high-quality patterns have excellent sub-50-nm resolution, and approach the mesopore regime. The compatibility of X-ray and electron-beam lithography with existing micro- and nanofabrication processes will facilitate the integration of MOFs in miniaturized devices.

To structure matter at the (sub-)nanometre scale, both bottom-up and top-down strategies are pursued. Bottom-up approaches inspired by biological systems seek to have molecular building blocks self-assemble into a desired arrangement. However, precise control over the localization of the self-assembly sites is a challenging task[1]. In contrast, top-down approaches use external stimuli to remove the undesired parts of a larger area to create the desired shapes in the preferred location[2]. The convergence of self-assembly and top-down approaches would lead to multiscale control over the organization of matter, from arranging molecular building blocks to shaping the materials they form[2–4]. For instance, high-resolution patterning can be achieved by using lithographically defined guiding patterns to direct the self-assembly of engineered block copolymers[5]. In this case, self-assembly serves solely to achieve smaller-pitch patterns, since the block copolymer is sacrificed. An anticipated next step in bringing together bottom-up and top-down approaches is the patterning and integration of self-assembled materials as functional components.

MOFs are porous materials that form through the self-assembly of metal-ion nodes and multitopic organic linkers[6,7]. Because of their porous and modular nature, MOFs offer unique prospects in micro- and optoelectronics, such as low-*k* dielectrics, light-emitting diodes and chemical sensors[8–12]. Thin-film deposition and patterning are the fundamental steps to integrate any novel material into a miniaturized device. However, patterning techniques for MOFs are still in their infancy and suffer from low resolution and poorly defined pattern edges (Supplementary Information Section 1)[12,13]. In conventional lithography, the pattern generated in a resist layer is etched into a film of the material of interest, followed by stripping of the resist mask[14]. The few reported examples of lithographic MOF patterning follow this approach[15–19]. Direct, resist-free lithography of functional materials is desirable to minimize the number of process steps and possible contamination sources, especially for highly porous materials[20–23]. For instance, direct patterning of porous low-*k* dielectrics could eliminate resist contamination and the exposure to damaging plasma[23,24]. Herein, we report resist-free lithography of MOFs at the micro- and nanoscale by X-ray and electron-beam lithography (XRL and EBL, respectively; Fig. 1). This straightforward approach enables high-quality MOF patterns in which all desirable material properties are maintained. A high-quality edge and a sub-50-nm resolution are demonstrated, both substantial improvements over previously reported lithographic MOF patterns[15–19]. Furthermore, we demonstrate the suitability of this approach to the fabrication of photonic gas sensors by patterning MOF films into highly regular diffractive optical structures.

X-ray lithography of ZIF thin films

In XRL, a mask is used to pattern an X-ray-sensitive layer with a resolution down to 100 nm[25]. In contrast, EBL is a maskless technique based on direct writing in an electron-beam-sensitive material, with a resolution extending below 10 nm[26]. In both techniques, the solubility of the irradiated area changes, which enables selective dissolution of either the exposed or the non-exposed region during the developing step (Fig. 1b). To evaluate the feasibility of direct lithography of MOFs, we screened the X-ray sensitivity of a variety of zeolitic imidazolate frameworks (ZIFs[27], a subclass of MOFs) by exposing ZIF powders to X-rays (2–30 keV; Supplementary Information Section 2). Among the investigated ZIFs, all halogenated materials, including ZIF-71, ZIF-71-Co, ZIF-72 and ZIF-8 with 4,5-dichloroimidazole (dc-im), 2-chloroimidazole (Cl-im) and 2-bromoimidazole (Br-im) linkers (Fig. 1a), exhibited a clear solubility switch from a threshold dose onwards, regardless of their topology or structural metal ion. While the pristine halogenated

[1]Centre for Membrane Separations, Adsorption, Catalysis, and Spectroscopy for Sustainable Solutions (cMACS), KU Leuven, Leuven, Belgium. [2]Research Group of Electrochemical and Surface Engineering, Department of Materials and Chemistry, Vrije Universiteit Brussel, Brussels, Belgium. [3]Division of Molecular Imaging and Photonics, Department of Chemistry, KU Leuven, Leuven, Belgium. [4]Catalysis Research Centre, Technical University of Munich, Garching, Germany. [5]Institute of Inorganic Chemistry, Graz University of Technology, Graz, Austria. [6]Institute of Physical and Theoretical Chemistry, Graz University of Technology, Graz, Austria. [7]School of Physical Sciences, Faculty of Sciences, University of Adelaide, Adelaide, South Australia, Australia. ✉e-mail: rob.ameloot@kuleuven.be

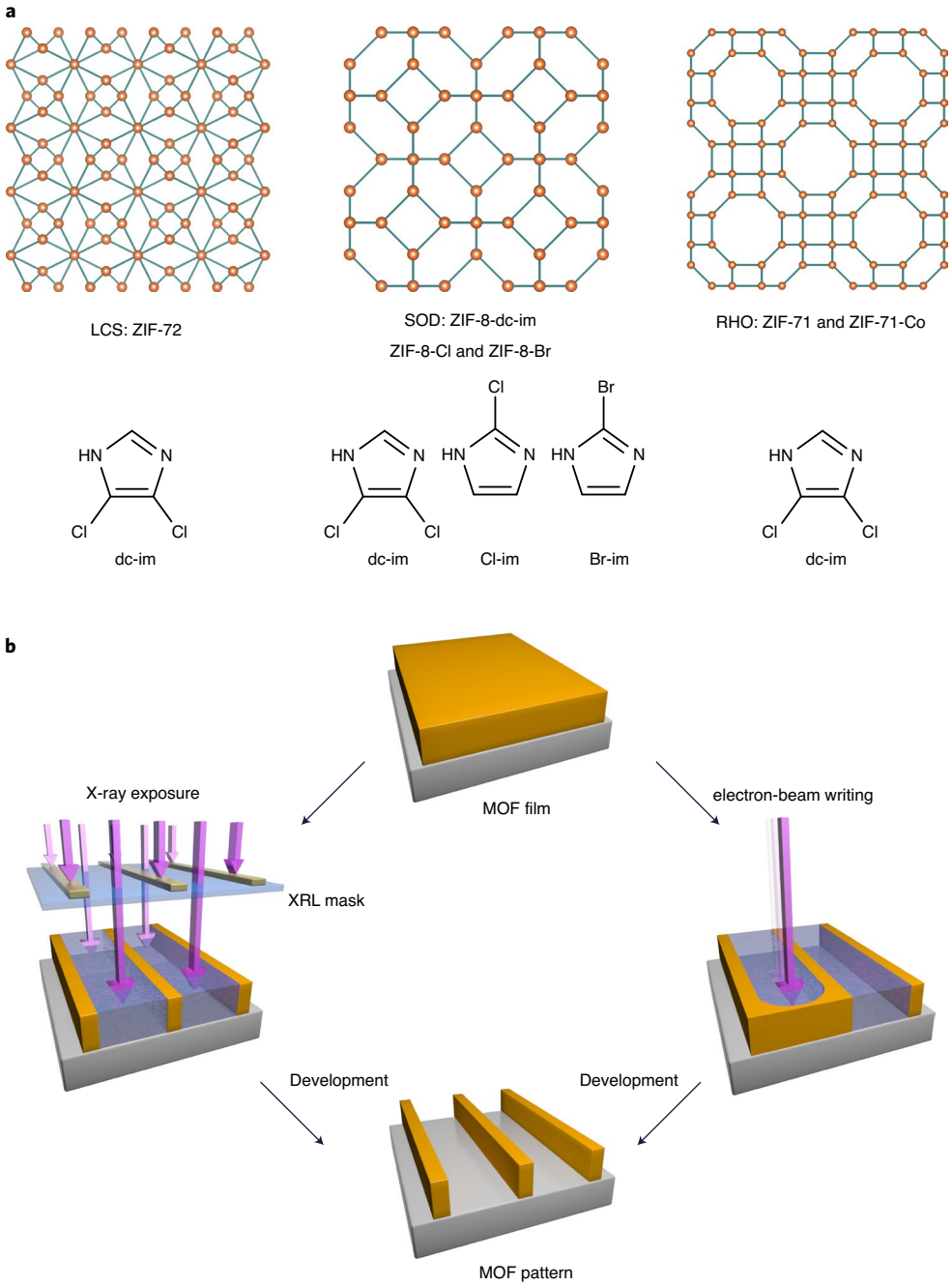

Fig. 1 | Direct patterning of MOF films by XRL and EBL. a, Ball-and-stick representation of halogenated ZIFs that are directly patterned by XRL and EBL (top). Capitalized three-letter codes correspond to the ZIF topologies. Cl-im, Br-im and dc-im represent the 2-chloroimidazole, 2-bromoimidazole and 4,5-dichloroimidazole linkers, respectively (structures shown below corresponding ZIFs). All ZIFs are zinc-based except ZIF-71-Co. **b**, Schematic illustration of direct patterning of MOF films by XRL and EBL. The MOF film is irradiated by X-rays through a mask (XRL) or by direct electron-beam writing (EBL). The pattern is developed by removing the irradiated part in DMSO.

ZIFs are entirely insoluble in dimethylsulfoxide (DMSO), they readily dissolve in this solvent after X-ray irradiation (Supplementary Fig. 4). In contrast, non-halogenated ZIFs do not show solubility changes in any common solvent (Supplementary Fig. 4), although a loss of crystallinity occurs at high X-ray doses (Supplementary Fig. 5), consistent with a previous report[28].

To further evaluate halogenated ZIFs as positive-tone materials in direct lithography, films were grown by chemical vapour deposition. The two-step MOF chemical vapour deposition process consists of depositing a ZnO precursor layer and subsequently converting it to the desired ZIF film in an imidazole linker atmosphere[16]. The ZIF films were characterized by grazing-incidence small-angle X-ray scattering (GISAXS), scanning electron microscopy (SEM), atomic force microscopy (AFM) and ellipsometry (Supplementary Information Section 3). To evaluate the lithographic process, an XRL mask with dots and holes of different shapes and dimensions was used (ranging from 10 to 150 μm; Supplementary Fig. 2). Taking 300 nm ZIF-71 films as an illustration case, the optimal volume dose was found to be 60 kJ cm^{-3}. The crystal structure of non-irradiated ZIF-71 is maintained throughout the XRL

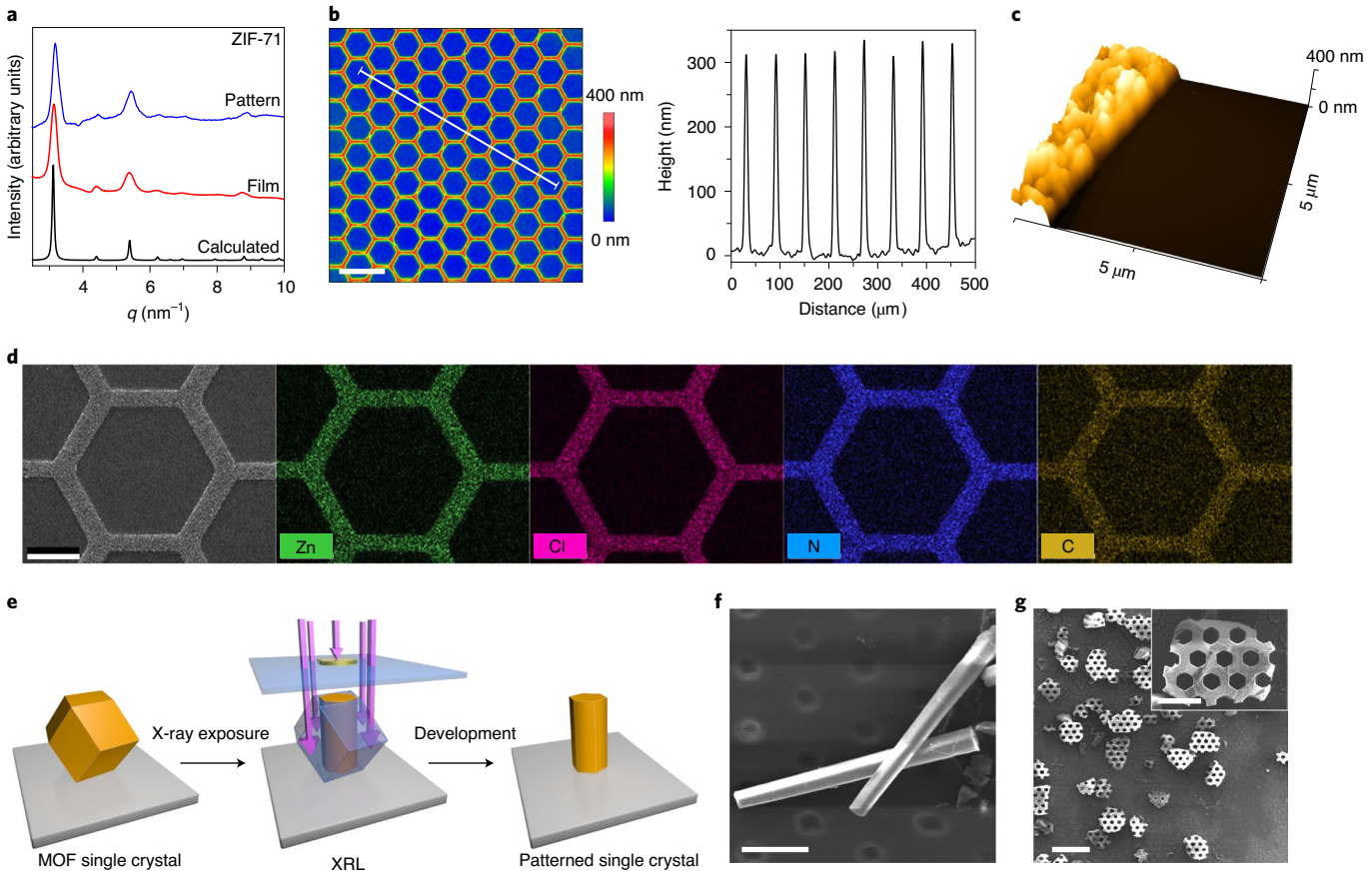

Fig. 2 | Halogenated ZIF films and single crystals after XRL patterning. a, Synchrotron GISAXS patterns of 300 nm thick ZIF-71 films before and after XRL and comparison with the calculated ZIF-71 powder X-ray diffraction pattern. **b**, Optical profilometry of the patterned ZIF-71 film (left, scale bar 100 μm) and the line profile extracted from this image (right). **c**, AFM topographic image of the edge of the ZIF-71 pattern. **d**, SEM-EDX mapping (zinc, chlorine, nitrogen and carbon) of the patterned ZIF-71 film. Scale bar 20 μm. **e**, Schematic illustration of the direct patterning of MOF single crystals by XRL. **f**,**g**, SEM images of ~100 μm ZIF-8-dc-im single crystals after XRL patterning with a negative (**f**) and positive (**g**) hexagonal grid mask. The resulting particles retain their single-crystalline nature. Scale bars: **f**, 20 μm; **g**, 200 μm and 50 μm for inset.

process, as confirmed by GISAXS (Fig. 2a). Through the removal of the irradiated areas, even the smallest features of the mask are replicated with high fidelity in the ZIF-71 layer (Fig. 2b). Profilometry together with energy-dispersive X-ray spectroscopy (EDX) mapping indicates that the irradiated area is completely removed, as further confirmed by AFM (Fig. 2b–d). Furthermore, both AFM and SEM demonstrate the sharp edges of the ZIF-71 pattern (Fig. 2c and Extended Data Fig. 1). Besides ZIF-71, the same XRL protocol can be employed for the direct patterning of different halogenated ZIF films, with similar optimal exposure doses (60–100 kJ cm^{-3}; Supplementary Information Section 4).

X-ray lithography of ZIF single crystals

XRL is capable of patterning thick layers (up to millimetres) due to the deep penetration of the high-energy X-rays[29]. To leverage this capability, XRL was performed on 50–200 μm ZIF-8-dc-im single crystals (Fig. 2e). Positive and negative hexagonal grid masks enable clean slicing through the entire crystal, in a 'cookie cutter' fashion, to yield crystals with hexagonal holes and freestanding hexagonal rods, respectively (Fig. 2f,g and Extended Data Fig. 2). To validate the retention of the single-crystalline nature of these particles, single-crystal X-ray diffraction was conducted. The starting ZIF-8-dc-im crystallizes in the cubic *Im*-3*m* space group[30]. Remarkably, the diffraction patterns of the single crystals after XRL are of high enough quality to determine that the unit cell parameters are identical to those of the starting crystals (Supplementary Table 3), thus demonstrating that the single-crystalline nature is maintained after XRL patterning. This patterning approach could enable cutting crystals into the desired morphology (for example, slices along crystallographic planes) and obtaining hierarchical structures with ordered porosity at multiple length scales for a range of applications[31,32].

X-ray-induced changes in ZIFs

The initially white halogenated ZIF powders turn brown upon X-ray exposure (Supplementary Fig. 4), indicating a chemical change in the materials. X-ray-induced changes typically comprise primary and secondary phenomena. Primary bond breaking occurs because of the interactions between the X-rays and the irradiated material through photoelectric, Compton or Auger effects[28]. Secondary reactions result from radiolytic products such as free radicals generated by the energetic electrons[33,34]. Since halogenated ZIFs undergo both decomposition and a solubility switch, while non-halogenated ZIFs exhibit only loss of crystallinity (Supplementary Figs. 4–6)[28], halogen atoms on the structural linkers evidently play a vital role in these processes. GISAXS data show that ZIF-71 films lose their crystallinity at X-ray doses over 5 kJ cm^{-3}, while a dose higher than 60 kJ cm^{-3} is required for a complete solubility switch (Fig. 3a). While the solution ^{1}H NMR spectrum of the pristine dc-im linker has only one peak, at ~7.5 ppm, a large number of peaks appear

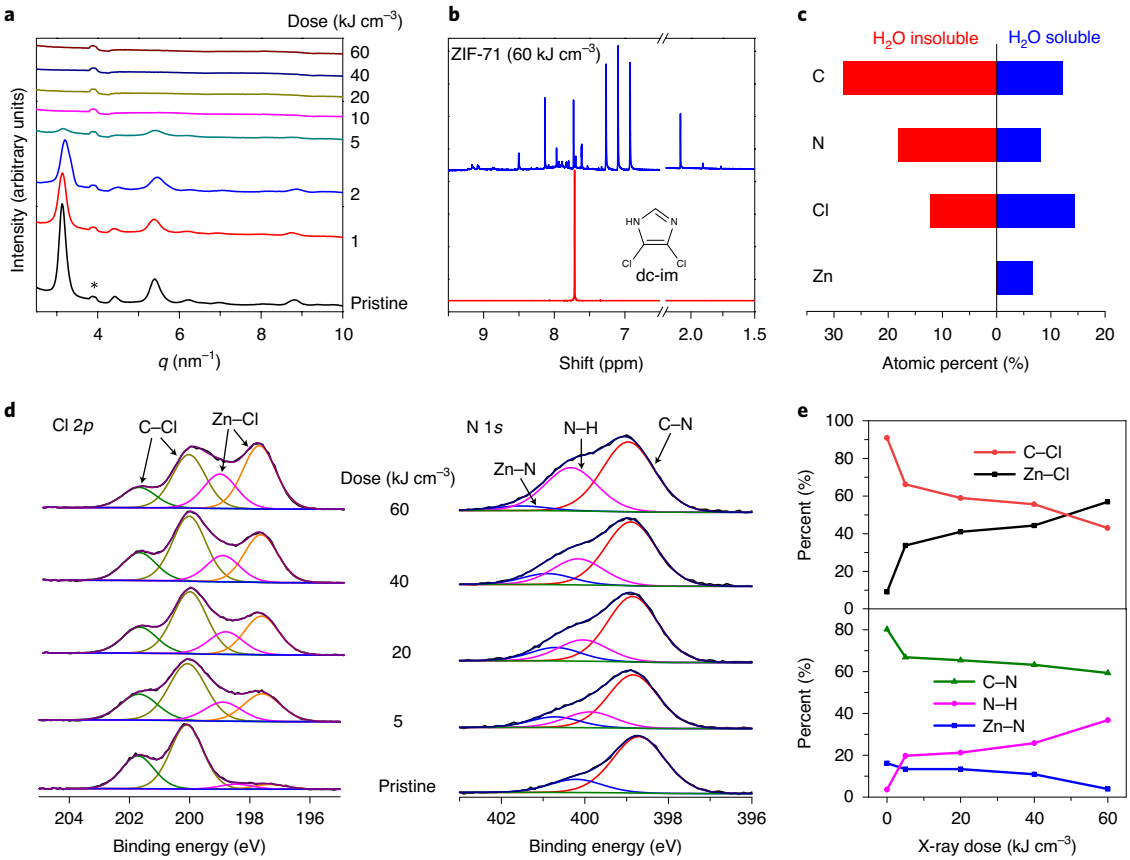

Fig. 3 | Mechanistic investigation of the X-ray dose on ZIF-71. a, Ex situ synchrotron GISAXS patterns of a ZIF-71 film as a function of X-ray dose. The asterisk indicates a detector artefact. **b**, Solution ^{1}H NMR spectra of dc-im linker (red) and X-ray irradiated ZIF-71 powder (60 kJ cm^{-3}, blue) in DMSO-d_6. **c**, Elemental analysis of the water-soluble and water-insoluble fractions of ZIF-71 powder after X-ray exposure (60 kJ cm^{-3}). **d**, XPS chlorine 2*p* and nitrogen 1s spectra of a ZIF-71 film as a function of X-ray dose. **e**, The proportion of chlorine bonds (C-Cl and Zn-Cl, top) and nitrogen bonds (C-N, N-H and Zn-N, bottom) as a function of X-ray dose, calculated from the ratio of integrated areas of the XPS spectra.

in the 6.5–9 ppm and 2.5–1.5 ppm ranges after X-ray irradiation (Fig. 3b). These peaks indicate bond cleavage of the imidazolate linker and the formation of different imines, C–H bonds or amines. These chemical changes are likely induced by chlorine radicals that are sufficiently reactive to initiate C–H activation, C–C bond cleavage and ring-opening reactions[35–37].

The X-ray-induced changes of ZIF-71 films were further studied by X-ray photoelectron spectroscopy (XPS). No obvious changes are found in the zinc 2*p* spectra, indicating no reduction of Zn^{2+} (Supplementary Fig. 44)[38]. In the nitrogen 1*s* XPS spectra, the sub-peaks related to C–N and Zn–N bonds decrease along with an increase in the N–H bond signal[39], suggesting the cleavage of the C–N bonds in the imidazolate ring and the framework Zn–N bonds (Fig. 3d, e). The decrease of C–Cl bond signal together with the rise of the Zn–Cl bond signal suggests the formation of chlorine radicals by the homolysis of C–Cl bonds (Fig. 3d, e)[40]. These chlorine radicals likely initiate the cleavage of the C–C, C–N and Zn–N bonds, resulting in further reactions (for example, Zn–Cl bond formation) between the formed fragments. The formation of zinc–halide bonds has also been observed as a result of the thermal treatment of halogenated ZIFs[41]. No change in composition is observed (Supplementary Table 4), suggesting that negligible material is lost through volatilization during X-ray exposure. Fig. 3c displays the elemental analysis of the water-soluble and water-insoluble fractions of X-ray-irradiated ZIF-71. Both fractions contain carbon, nitrogen and chlorine, while only the water-soluble fraction contains zinc. The water-soluble fraction may consist of Zn-Cl salts (for example, $ZnCl_2$) and Zn-N or Cl-Zn-N complexes. It is proposed that the water-insoluble but DMSO-soluble fraction consists of a partially polymerized organic fraction, which might be initiated by the Lewis acid $ZnCl_2$ (ref. [42]). In contrast, the imidazolate linkers of non-halogenated ZIFs remain intact upon X-ray-induced amorphization[28]. Therefore, the crucial role of the halogen atoms is to enable fragmentation of the imidazolate linker, thus permitting dissolution and direct lithography (Supplementary Information Section 5). We anticipate that MOFs based on other halogenated heterocyclic linkers may show similar lability to X-rays, thus enabling direct lithography. Moreover, the different behaviour of halogenated and non-halogenated linkers opens an avenue towards selective removal, through XRL, of halogenated linkers in MOFs containing both types (for example, mixed-linker MOFs, core-shell structures or bilayer films), resulting in complex architectures currently not accessible[43].

Electron-beam lithography of ZIFs

XRL resists can often also be applied in EBL, since the electron beam has the same effect as the photoelectrons generated by the X-rays[44]. It was previously observed that repeated scanning during electron microscopy can induce amorphization of non-halogenated ZIFs, resulting in a less soluble amorphous deposit[45]. Analogously to the different behaviour of non-halogenated and halogenated ZIFs in XRL, the latter behave as positive-tone materials in direct EBL. The optimal electron-beam area dose for ZIF-71 patterning was found to be ~1,000 μC cm^{-2} (Supplementary Figs. 51,52). The irradiated

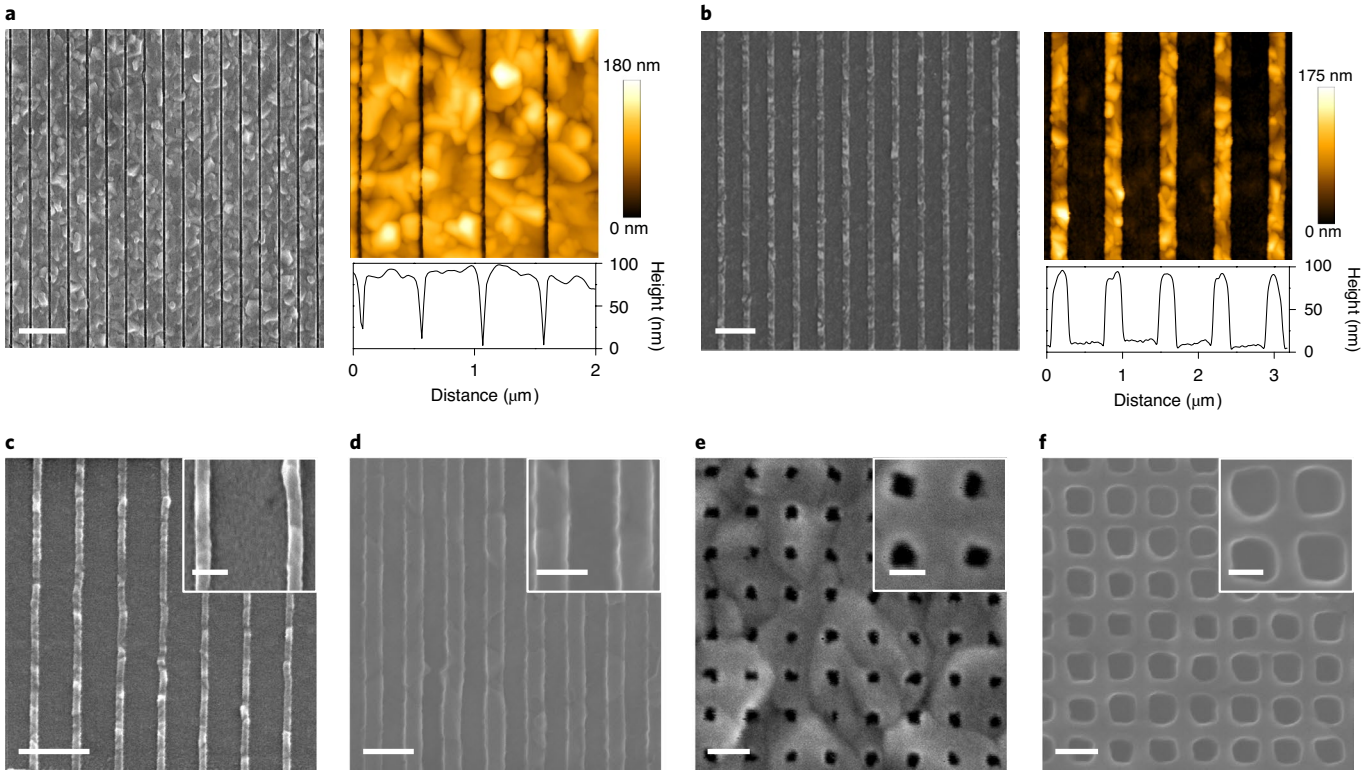

Fig. 4 | High-resolution EBL patterning of 100 nm thick ZIF-71 films. a,**b**, SEM (left) and AFM (right) topographic images of the ZIF-71 film with 50 nm trenches (**a**) and 200 nm lines (**b**). **c**,**d** SEM images of the ZIF-71 film with 100 nm (**c**) and 60 nm (**d**) lines. **e**,**f**, SEM images of the ZIF-71 film with 40 nm holes (**e**) and a grid with a 30 nm line width (**f**). Scale bars: **a**,**b**, 1 μm; **c**, 1 μm (200 nm for inset); **d**, 200 nm (100 nm for inset); **e**,**f**, 100 nm (50 nm for inset).

part cannot be developed completely at lower irradiation doses, while higher doses result in a mismatch between the developed and exposed areas due to electron scattering of the primary, secondary and backscattered electrons[46]. Patterns with different shapes and feature sizes were obtained by direct electron-beam writing in a 100 nm thick ZIF-71 film and subsequent development in DMSO (Supplementary Information Section 6). Straight lines with sharp edges can be achieved for features down to 50 nm (Fig. 4a–d and Extended Data Fig. 3). In all patterns, the ZIF-71 crystal facets remain clearly visible, suggesting that the patterned MOF remained intact, as during XRL. AFM data (Fig. 4b) suggest that most of the irradiated area is developed, except for a small residue that probably formed by electron-beam-induced crosslinking of linker fragments[47]. High-resolution patterning with features below 50 nm can be realized, although the pattern edge quality deteriorates because of the proximity effect (Fig. 4e,f and Supplementary Fig. 59). The proximity effect can become more pronounced for even higher resolutions. Minimizing these effects will require systematic optimization of patterning parameters, including the beam energy and current, field parameters and deflection mode[48].

Porosity of patterned ZIF thin films

To leverage MOFs in solid-state devices, patterning should not alter their physicochemical properties, especially their porosity. Notably, previous studies[12,13] have not tested this assumption. The porosity of patterned ZIF-71 films was studied by krypton and methanol physisorption on MOF-coated micropillar arrays and quartz crystal microbalance (QCM) substrates, respectively (Fig. 5a–d). The MOF chemical vapour deposition process enables conformal ZIF-71 coatings on the pillar arrays, resulting in a geometric surface area enhancement that enables krypton sorption measurements (Supplementary Fig. 32)[16]. The resulting type I isotherm and the Brunauer–Emmett–Teller (BET) surface area per film area of 247 $m^2 m^{-2}$ demonstrate the microporous nature of the ZIF-71 coating before X-ray irradiation (Fig. 5c). Based on the calculated ZIF-71 density (1.17 $g cm^{-3}$) and measured film thickness (200 nm), a specific BET surface area of 1,055 $m^2 g^{-1}$ is found, which is similar to the value reported for powder samples[49]. After X-ray irradiation and removal of the coating on half of the pillar array, the BET surface area of the remaining ZIF-71 film was virtually unchanged (236 $m^2 m^{-2}$; Fig. 5c). Gravimetric QCM monitoring shows an S-shaped methanol adsorption isotherm (Fig. 5d), in good agreement with data reported for a ZIF-71 powder sample[50]. By using the removed film fraction as a correction factor, the gravimetric methanol isotherms of the patterned and unpatterned ZIF-71 films nearly overlap. These results illustrate that the ZIF-71 film remaining after XRL fully retains its porosity. Moreover, the successful polymerization of poly(3,4-ethylenedioxythiophene) (PEDOT) in the ZIF-71 EBL pattern confirms that the patterned MOF is porous (Supplementary Fig. 65).

Adsorption in the MOF pores makes it possible to concentrate analyte molecules. High-resolution patterning of MOF films offers new opportunities for the fabrication of chemical sensors, by enabling the transduction of guest adsorption to an optical signal without relying on luminescence[11]. Due to their spatial periodicity in refractive index, ZIF-71 patterns on a transparent substrate act as diffraction phase gratings for light in the visible range (Fig. 5e,f)[51]. When guest molecules adsorb in the pores, the phase difference resulting from the ZIF-71 pattern increases together with the refractive index of the MOF layer. Therefore, guest adsorption can be monitored through the intensity changes of the first-order diffraction spots[51]. This principle is illustrated for methanol vapour sensing using a 200 nm thick ZIF-71 diffraction grating covering a 4 × 4 mm^2 area (Fig. 5g,h). The resulting sensing data are in excellent

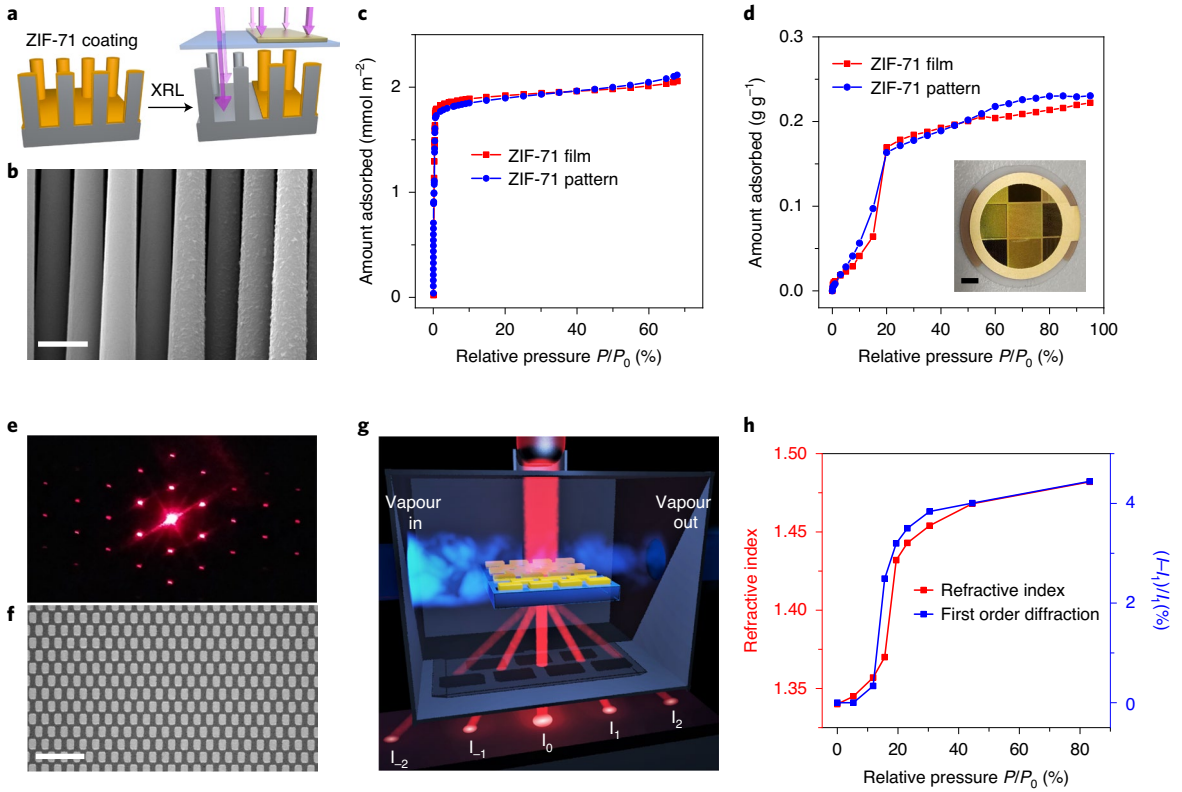

Fig. 5 | Porosity characterization and sensing application of patterned ZIF-71 films. a, Scheme of XRL patterning of a ZIF-71-coated silicon pillar array for krypton physisorption. **b**, Cross-sectional SEM image of a silicon pillar array after removal of the ZIF-71 film in the left half. Scale bar 5 µm. **c**, Krypton adsorption isotherms of ZIF-71-coated silicon pillar arrays before and after XRL. The uptake values per square metre of MOF are plotted by considering only the MOF-covered area for the patterned pillar array. **d**, Methanol adsorption isotherms of ZIF-71-coated QCM substrates before and after XRL. Specific uptake values per gram of MOF are plotted by taking only the MOF-covered area into account for the patterned film. The inset shows a photograph of the ZIF-71 pattern on a QCM substrate. Each square consists of a different microstructure. Scale bar 2 mm. **e**, Picture of the diffraction pattern resulting from illuminating a ZIF-71 pattern on quartz with a red laser pointer. **f**, Optical microscopy image of the corresponding patterned ZIF-71 film acting as a diffraction grating. Scale bar 100 µm. **g**, Scheme of the evaluation of ZIF-71 patterns as diffraction grating vapour sensors. **h**, Evolution of the refractive index of a ZIF-71 film measured by ellipsometry (red) and the normalized intensity of the first-order diffraction spot (I_1) of the ZIF-71 grating (blue) as a function of methanol vapour pressure.

agreement with the in situ ellipsometry and QCM reference adsorption experiments. Despite its simplicity, this example illustrates the potential of scalable high-resolution patterning of MOF films for gas sensing (Supplementary Information Section 7). Apart from their potential in sensing, MOFs are candidates for future low-k dielectrics. The uniformly distributed pores in crystalline MOFs can improve the balance of Young's modulus and dielectric constant[9,10,52]. However, for porous low-k materials, the conventional damascene integration approach is challenging, due to plasma damage and resist contamination[23,24]. Considering the advantages of the direct patterning approach, we proposed an alternative strategy to integrate MOFs as low-k dielectrics into on-chip interconnects that may overcome these challenges (Supplementary Information Section 8).

Outlook

We demonstrated the direct lithographic patterning of MOFs without the use of resist layers. This approach enables a resolution approaching the mesopore regime, while preserving the crystallinity and porosity of the patterned MOFs. The compatibility of XRL and EBL with micro- and nanofabrication provides a new perspective on the potential of MOFs as high-performance dielectrics, coatings for more selective and sensitive sensors, luminescent pixels for display technology and so on. Looking ahead, such integrations could be accelerated through extreme ultraviolet lithography, a state-of-the-art method in which a solubility switch mechanism similar to the one reported here is expected.

Online content

Any methods, additional references, Nature Research reporting summaries, source data, extended data, supplementary information, acknowledgements, peer review information; details of author contributions and competing interests; and statements of data and code availability are available at https://doi.org/10.1038/s41563-020-00827-x.

Received: 11 April 2020; Accepted: 14 September 2020;
Published online: 26 October 2020

References

1. Aizenberg, J., Black, A. J. & Whitesides, G. M. Control of crystal nucleation by patterned self-assembled monolayers. *Nature* **398**, 495–498 (1999).
2. Liddle, J. A. & Gallatin, G. M. Nanomanufacturing: a perspective. *ACS Nano* **10**, 2995–3014 (2016).
3. Isaacoff, B. P. & Brown, K. A. Progress in top-down control of bottom-up assembly. *Nano Lett.* **17**, 6508–6510 (2017).
4. Smith, K. H., Tejeda-Montes, E., Poch, M. & Mata, A. Integrating top-down and self-assembly in the fabrication of peptide and protein-based biomedical materials. *Chem. Soc. Rev.* **40**, 4563–4577 (2011).

5. Liu, C.-C. et al. Directed self-assembly of block copolymers for 7 nanometre FinFET technology and beyond. *Nat. Electron.* **1**, 562–569 (2018).
6. Batten, S. R. et al. Terminology of metal–organic frameworks and coordination polymers (IUPAC Recommendations 2013). *Pure Appl. Chem.* **85**, 1715–1724 (2013).
7. Bennett, T. D. & Horike, S. Liquid, glass and amorphous solid states of coordination polymers and metal–organic frameworks. *Nat. Rev. Mater.* **3**, 431–440 (2018).
8. Usman, M., Mendiratta, S. & Lu, K.-L. Semiconductor metal–organic frameworks: future low-bandgap materials. *Adv. Mater.* **29**, 1605071 (2017).
9. Krishtab, M. et al. Vapor-deposited zeolitic imidazolate frameworks as gap-filling ultra-low-*k* dielectrics. *Nat. Commun.* **10**, 3729 (2019).
10. Ryder, M. R. et al. Dielectric properties of zeolitic imidazolate frameworks in the broad-band infrared regime. *J. Phys. Chem. Lett.* **9**, 2678–2684 (2018).
11. Lustig, W. P. et al. Metal–organic frameworks: functional luminescent and photonic materials for sensing applications. *Chem. Soc. Rev.* **46**, 3242–3285 (2017).
12. Stassen, I. et al. An updated roadmap for the integration of metal–organic frameworks with electronic devices and chemical sensors. *Chem. Soc. Rev.* **46**, 3185–3241 (2017).
13. Falcaro, P. et al. MOF positioning technology and device fabrication. *Chem. Soc. Rev.* **43**, 5513–5560 (2014).
14. Ito, T. & Okazaki, S. Pushing the limits of lithography. *Nature* **406**, 1027–1031 (2000).
15. Lu, G., Farha, O. K., Zhang, W., Huo, F. & Hupp, J. T. Engineering ZIF-8 thin films for hybrid MOF-based devices. *Adv. Mater.* **24**, 3970–3974 (2012).
16. Stassen, I. et al. Chemical vapour deposition of zeolitic imidazolate framework thin films. *Nat. Mater.* **15**, 304–310 (2016).
17. Okada, K. et al. Copper conversion into $Cu(OH)_2$ nanotubes for positioning $Cu_3(BTC)_2$ MOF crystals: controlling the growth on flat plates, 3D architectures, and as patterns. *Adv. Funct. Mater.* **24**, 1969–1977 (2014).
18. Dalstein, O. et al. Nanoimprinted, submicrometric, MOF-based 2D photonic structures: toward easy selective vapors sensing by a smartphone camera. *Adv. Funct. Mater.* **26**, 81–90 (2016).
19. Razmjou, A. et al. Preparation of iridescent 2D photonic crystals by using a mussel-inspired spatial patterning of ZIF-8 with potential applications in optical switch and chemical sensor. *ACS Appl. Mater. Interfaces* **9**, 38076–38080 (2017).
20. Wang, Y., Fedin, I., Zhang, H. & Talapin, D. V. Direct optical lithography of functional inorganic nanomaterials. *Science* **357**, 385–388 (2017).
21. Garcia, R., Knoll, A. W. & Riedo, E. Advanced scanning probe lithography. *Nat. Nanotechnol.* **9**, 577–587 (2014).
22. Nakayama, K. et al. High-mobility organic transistors with wet-etch-patterned top electrodes: a novel patterning method for fine-pitch integration of organic devices. *Adv. Mater. Interfaces* **1**, 1300124 (2014).
23. Kumar, R., Singh, N., Chang, C. K., Dong, L. & Wong, T. K. S. Deep-ultraviolet resist contamination for copper/low-*k* dual-damascene patterning. *J. Vac. Sci. Technol. B* **22**, 1052 (2004).
24. Baklanov, M. R. et al. Plasma processing of low-*k* dielectrics. *J. Appl. Phys.* **113**, 041101 (2013).
25. Maldonado, J. R. & Peckerar, M. X-ray lithography: some history, current status and future prospects. *Microelectron. Eng.* **161**, 87–93 (2016).
26. Chen, Y. Nanofabrication by electron beam lithography and its applications: a review. *Microelectron. Eng.* **135**, 57–72 (2015).
27. Banerjee, R. et al. High-throughput synthesis of zeolitic imidazolate frameworks and application to CO_2 capture. *Science* **319**, 939–943 (2008).
28. Widmer, R. N. et al. X-ray radiation-induced amorphization of metal–organic frameworks. *Phys. Chem. Chem. Phys.* **21**, 12389–12395 (2019).
29. Innocenzi, P., Malfatti, L., Marmiroli, B. & Falcaro, P. Hard X-rays and soft-matter: processing of sol–gel films from a top down route. *J. Solgel Sci. Technol.* **70**, 236–244 (2014).
30. Schweinefuß, M. E. et al. Zeolitic imidazolate framework-71 nanocrystals and a novel SOD-type polymorph: solution mediated phase transformations, phase selection via coordination modulation and a density functional theory derived energy landscape. *Dalton Trans.* **43**, 3528–3536 (2014).
31. Shen, K. et al. Ordered macro–microporous metal–organic framework single crystals. *Science* **359**, 206–210 (2018).
32. Luo, Y., Ahmad, M., Schug, A. & Tsotsalas, M. Rising up: hierarchical metal–organic frameworks in experiments and simulations. *Adv. Mater.* **31**, 1901744 (2019).
33. Choi, J. O., Moore, J. A., Corelli, J. C., Silverman, J. P. & Bakhru, H. Degradation of poly(methylmethacrylate) by deep ultraviolet, x-ray, electron beam, and proton beam irradiations. *J. Vac. Sci. Technol. B* **6**, 2286–2289 (1988).
34. Ihee, H. et al. Ultrafast X-ray diffraction of transient molecular structures in solution. *Science* **309**, 1223–1227 (2005).
35. Yuan, R. et al. Chlorine-radical-mediated photocatalytic activation of C–H bonds with visible light. *Angew. Chem. Int. Ed.* **52**, 1035–1039 (2013).
36. Lewandowski, M. & Ollis, D. F. Halide acid pretreatments of photocatalysts for oxidation of aromatic air contaminants: rate enhancement, rate inhibition, and a thermodynamic rationale. *J. Catal.* **217**, 38–46 (2003).
37. Sivaguru, P., Wang, Z., Zanoni, G. & Bi, X. Cleavage of carbon–carbon bonds by radical reactions. *Chem. Soc. Rev.* **48**, 2615–2656 (2019).
38. Cruz, A. J. et al. Integrated cleanroom process for the vapor-phase deposition of large-area zeolitic imidazolate framework thin films. *Chem. Mater.* **31**, 9462–9471 (2019).
39. Japip, S., Liao, K.-S., Xiao, Y. & Chung, T.-S. Enhancement of molecular-sieving properties by constructing surface nano-metric layer via vapor cross-linking. *J. Membr. Sci.* **497**, 248–258 (2016).
40. Taylor, A. W., Men, S., Clarke, C. J. & Licence, P. Acidity and basicity of halometallate-based ionic liquids from X-ray photoelectron spectroscopy. *RSC Adv.* **3**, 9436–9445 (2013).
41. Hou, J. et al. Halogenated metal–organic framework glasses and liquids. *J. Am. Chem. Soc.* **142**, 3880–3890 (2020).
42. Saitoh, R., Kanazawa, A., Kanaoka, S. & Aoshima, S. Cationic polymerization of *p*-methylstyrene using various metal chlorides: design rationale of initiating systems for controlled polymerization of styrenes. *Polym. J.* **48**, 933–940 (2016).
43. Furukawa, S., Reboul, J., Diring, S., Sumida, K. & Kitagawa, S. Structuring of metal–organic frameworks at the mesoscopic/macroscopic scale. *Chem. Soc. Rev.* **43**, 5700–5734 (2014).
44. Gangnaik, A. S., Georgiev, Y. M. & Holmes, J. D. New generation electron beam resists: a review. *Chem. Mater.* **29**, 1898–1917 (2017).
45. Conrad, S. et al. Controlling dissolution and transformation of zeolitic imidazolate frameworks by using electron-beam-induced amorphization. *Angew. Chem. Int. Ed.* **57**, 13592–13597 (2018).
46. Seo, E., Choi, B. K. & Kim, O. Determination of proximity effect parameters and the shape bias parameter in electron beam lithography. *Microelectron. Eng.* **53**, 305–308 (2000).
47. Nathawat, R., Kumar, A., Acharya, N. K. & Vijay, Y. K. XPS and AFM surface study of PMMA irradiated by electron beam. *Surf. Coat. Technol.* **203**, 2600–2604 (2009).
48. Li, K. et al. High speed e-beam writing for large area photonic nanostructures—a choice of parameters. *Sci. Rep.* **6**, 32945 (2016).
49. Khay, I. et al. Assessment of the energetic performances of various ZIFs with SOD or RHO topology using high pressure water intrusion–extrusion experiments. *Dalton Trans.* **45**, 4392–4400 (2016).
50. Zhang, K. et al. Alcohol and water adsorption in zeolitic imidazolate frameworks. *Chem. Commun.* **49**, 3245–3247 (2013).
51. Dalstein, O. et al. Evaporation-directed crack-patterning of metal–organic framework colloidal films and their application as photonic sensors. *Angew. Chem. Int. Ed.* **56**, 14011–14015 (2017).
52. Michalak, D. J. et al. Porosity scaling strategies for low-*k* films. *J. Mater. Res.* **30**, 3363–3385 (2015).

Methods

MOF thin-film deposition. Single-side polished and back-etched silicon wafers (Si-MAT) were used. Silicon pillar arrays with a diameter and height of 2 and 50 µm, respectively, were produced by deep reactive ion etching (Bosch process). The MOF film deposition consists of two steps: (1) deposition of the ZnO precursor layer by atomic layer deposition (ALD) and (2) vapour–solid conversion of the ZnO layer in an organic linker atmosphere. The ZnO films were deposited using a Savannah S-200 thermal ALD reactor (Veeco Instruments, Inc.) with deionized water and diethylzinc (deposition grade, Sigma-Aldrich) as precursors. The pulse and purge durations for the ALD precursors were set to 0.015 s and 5 s, respectively. The reactor base pressure was ~0.4 mbar at an N_2 gas flow of 20 sccm. This process resulted in a ZnO growth rate of 1.7 Å per cycle on silicon substrates at 120 °C. In the case of ZIF-71 deposition, ZnO film, 50 mg of dc-im (97%, TCI Europe) powder and a small quantity of *N*,*N*-dimethylformamide (50 µl, 99%, ARCOS Organics) were placed separately in a 250 ml Schlenk tube. After heating in a convection oven at 110 °C for 1 day, ZIF-71 film was obtained. ZIF-8-Cl-im and ZIF-8-Br-im were deposited by the same method but using Cl-im (97%, Sigma-Aldrich) and Br-im (97%, Sigma-Aldrich), respectively. The ZIF-72 film was deposited using dc-im at 150 °C without the addition of *N*,*N*-dimethylformamide. The obtained MOF films were activated by heating at 150 °C under dynamic vacuum (0.1 mbar) for 1 day.

X-ray lithography. XRL was performed at the DXRL beamline of Elettra synchrotron (Trieste, Italy)[53]. A scheme of the filter chamber and of the XRL scanner is shown in Supplementary Fig. 2. Samples can be directly exposed to the X-ray beam, or a mask containing patterns can be placed in front of the sample. The X-ray source is a bending magnet of 1.2 T, which has a characteristic energy of 3.22 KeV, and the radiation spectrum is composed of different energies (2–30 keV). The two main setups are the one for films deposited on flat substrates and the one for holding powders. The film sample holder is the standard one available in every XRL beamline. The powder sample holder consists of a 200 µm trench machined in a stainless steel block. The powder samples were irradiated by X-ray directly without a mask and were taken for further characterization. XRL patterning was performed by (1) irradiating the MOF film with X-rays through a mask composed of an X-ray transparent membrane (TiO_2, 2.2 µm thick) and an X-ray absorber (Au, 20 µm thick), (2) immersing the film in DMSO for 30 seconds (development) and (3) rinsing the film with acetone and drying with compressed air. The mask contains arrays of dots and holes with different shapes (squares, circles, hexagon and lines) with different dimensions (10–150 µm). A picture of the mask is shown in Supplementary Fig. 2. The patterning of ZIF-8-dc-im single crystals was performed in the film patterning mode by spreading out the crystals on double-sided Kapton tape. In XRL, the dose is commonly expressed as energy per unit volume absorbed at the bottom of the exposed material (traditionally expressed as kJ cm^{-3}). This takes into account the thickness of the material and its attenuation length (in the energy range of the X-ray beam spectrum). The typical X-ray doses for the patterning of ZIF-71, ZIF-8-Cl-im, ZIF-8-Br-im and ZIF-72 are 60, 80, 80 and 100 kJ cm^{-3}, respectively. Typically, for a 300 nm ZIF-71 film, the exposure time is 3 min at a ring energy of 2 GeV.

Electron-beam lithography. The EBL of MOF films was performed on a nanofabrication system from Raith GmbH. The working distance was set to 10 mm. The typical acceleration voltage was 20 kV. The beam current, measured by a Faraday cup, was in the range of 300–350 pA. The step sizes of the area and line doses were set to 10 nC cm^{-2} and 1,000 pC cm^{-1}, respectively. The patterns were written in a concentric, clockwise mode. After the electron-beam writing, the pattern was developed by immersing in DMSO for 30 s, rinsing with acetone and drying with compressed air.

Small-angle X-ray scattering. SAXS data were collected at the SAXS beamline at the Elettra synchrotron light source (Trieste, Italy) using a photon energy of 8 keV[54]. Images were recorded using the Pilatus3 1 M detector (DECTRIS Ltd.). The powder samples were recorded in capillary mode. The beamline setup was adjusted to a sample-to-detector distance of 757 mm to result in an available q range between 0.1 and 9.8 nm^{-1}. In the case of GISAXS, the beamline setup was adjusted to a sample-to-detector distance of 286 mm. A secondary vertical beamstop was used to safeguard the detector, resulting in an anisotropic q range of 0.1–25 nm^{-1}. All measurements were done at an incidence angle of 0.36°. The calibration and the calculation of the vertical slices were conducted using the FIT2D software package[55].

Single-crystal X-ray diffraction. SCXRD data were collected for pristine and patterned ZIF-8-dc-im crystals on a Bruker APEX II diffractometer with an Incoatec microfocus Mo-Kα tube (λ of 0.71073 Å) and a CCD (charge-coupled device) area detector. Empirical absorption corrections were applied using SADABS or TWINABS[56]. The structures were solved with the use of the intrinsic phasing option in SHELXT and refined by the full-matrix least-squares procedures in SHELXL[57]. The space group assignments and structural solutions were evaluated using PLATON[58]. Non-hydrogen atoms were refined anisotropically. Hydrogen atoms were located in calculated positions corresponding to standard bond lengths and angles and refined using a riding model. Atomic positions in the framework were evaluated by using the 'squeeze' option in the PLATON program suite[59].

Scanning electron microscopy. SEM images were recorded by using an FEI XL30FEG instrument after sputter-coating the samples with 5 nm platinum/palladium. The PEDOT@ZIF-71 pattern was coated by carbon for EDX analysis. EDX mapping was recorded by an EDAX detector with a resolution of 512×512 pixels.

Atomic force microscopy. AFM topography images (512×512 pixels) were recorded in intermittent contact mode using a PicoSPM (5100, Agilent Technologies) instrument at ambient conditions. Silicon cantilevers (OLYMPUS, AC160TS-R3) with resonance frequency around 300 kHz and spring constant around 26 N m^{-1} were used. Data analysis was performed using Gwyddion 2.44 and WSxM 5.0[60,61].

Optical profilometry. Optical profilometry images were recorded on a Sensofar 3D optical profilometer at ambient conditions. Data analysis was performed using Gwyddion 2.44 (ref. [60]).

Porosity study. Both N_2 and krypton sorption isotherms were measured at 77 K using a Micromeritics 3Flex physisorption instrument. The samples were degassed before measurements at 423 K under dynamic vacuum (1×10^{-2} mbar) for 12 h. The BET method was applied in the region between 0.005 and 0.05 P/P_0, according to the consistency criteria for microporous materials. Methanol adsorption isotherms on ZIF-71-coated QCM substrates were measured using a BEL-QCM instrument at 298 K (ref. [62]). The equilibrium time was set to 5 min. To study the porosity of the EBL-patterned sample, PEDOT was polymerized in the ZIF-71 pattern following a modified reported recipe[63]. First, 3,4-ethylenedioxythiophene (EDOT) was loaded into ZIF-71 film through vapour-phase loading by heating an evacuated Schlenk tube containing the ZIF-71 film and EDOT (100 µl, 97%, Sigma-Aldrich) at 90 °C for 6 h. Afterwards, the EDOT-loaded ZIF-71 film was exposed to I_2 (99.8%, Sigma-Aldrich) vapour at 50 °C for 6 h.

Ellipsometry. The optical properties of the deposited layers were measured using an M-2000x spectroscopic ellipsometer (J. A. Woollam Co. Inc., λ of 246–1,000 nm). A two-layer optical model was used, consisting of a native oxide layer and a MOF layer to be analysed. For MOF films, the Cauchy model was used with variable thickness and optical constants. The bare silicon substrates were measured to determine the thickness of the native oxide before every experiment. The ellipsometric parameters of the silicon substrate and the native oxide were taken from literature[64] and kept fixed for all measurements. In situ ellipsometry measurements were performed using a custom-built tool featuring a vacuum chamber, spectroscopic ellipsometer (iSE Woollam Ellipsometer, 400–1,000 nm wavelength) and a programmable adsorbate dosing platform. The isotherms were recorded at room temperature. The equilibration time at each pressure point was set to 5 min. The volumetric uptake is calculated based on the changes in refractive index (ellipsometric porosimetry)[65].

Diffraction grating vapour sensing. In the configuration of Fig. 5g, a phase difference (φ) is created when light passes through a MOF pattern deposited on a transparent substrate

$$\varphi = \frac{2\pi d(n_{\mathrm{MOF}} - n_{\mathrm{air}})}{\lambda} \quad (1)$$

in which φ is the phase difference, d is the MOF film thickness, n_{MOF} and n_{air} are the refractive indices of the MOF and the surrounding atmosphere, respectively, and λ is the wavelength of the incident beam. When guest molecules are adsorbed in the MOF pores, the larger refractive index difference (n_{MOF} increases because of the guest) causes a larger phase difference. Thus, guest adsorption can be transduced through monitoring the intensity changes of the first-order diffraction[66]

$$I_1 = \frac{2(1-\cos\varphi)}{\pi^2} \quad (2)$$

in which I_1 is the first-order diffraction intensity and φ is the phase difference of the grating. According to equations (1) and (2), for gratings with sub-micrometric thickness, the evolution of I_1 versus n is almost linear (Supplementary Fig. 70).

Vapour sensing was performed by illuminating MOF patterns on quartz substrates, horizontally positioned in a sealed enclosure (Linkam stage) connected to a vapour generating system. A 650 nm laser (Picotronic, modulated with adjustable focus) is used as a light source. The diffraction pattern is directly captured with a CMOS camera (Flir Chameleon 3, 2,048×1,536 pixels, monochrome, grating-sensor distance ~10 cm). During the dosing of methanol vapours, the intensity of a first-order diffraction spot was monitored every 2 s by integrating the CMOS response over a 136×136 pixel area around the diffraction spot (read by PySpin).

NMR spectroscopy. Solution ^{1}H NMR spectra were recorded on a Bruker Advance 300 MHz spectrometer. DMSO-d_6 was used as a solvent to dissolve the dc-im linker and X-ray irradiated ZIF-71 powder samples.

Elemental analysis. Elemental analyses for carbon, hydrogen and nitrogen were carried out on a Hekatech EuroEA Elemental Analyser. The zinc content was determined by atomic absorption spectroscopy after microwave decomposition of the sample in a mixture of sulfuric acid and nitric acid. The chlorine content was determined by potentiometric titration using an Agilent technologies 200 series AA instrument.

X-ray photoelectron spectroscopy. XPS data for X-ray irradiated ZIF-71 films were collected using a PHI5600 Versaprobe II (Physical Electronics) utilizing an aluminium Kα monochromatic X-ray source (1,486.71 eV photon energy) with a beam irradiation power of 25 W. The kinetic energy of the photoelectrons was measured with a take-off angle of 45° and a spot diameter of 100 µm. Survey and high-resolution scans were recorded with pass energies of 187.85 eV and 23.5 eV and step sizes of 0.1 eV and 0.05 eV, respectively. Dual-beam charge neutralization was used to compensate for potential charging effects. The analysis and fitting were performed using CasaXPS software (Casa Software, Ltd.) employing a mixed Gaussian-Lorentzian peak shape and a Shirley-type background. The probe depths for the films were found to be 3–5 nm when evaluated using the Tanuma, Powel and Penn (TPP-2M) relation[67].

Data availability

The data represented in Figs. 2a,b, 3 and 5c,d,h are provided with the paper as Source data. The image datasets are available from figshare (https://doi.org/10.6084/m9.figshare.12946922).

References

53. Pérennès, F., De Bona, F. & Pantenburg, F. J. Deep X-ray lithography beamline at Elettra. *Nucl. Instrum. Meth. A* **467–468**, 1274–1278 (2001).
54. Amenitsch, H. et al. First performance assessment of the small-angle X-ray scattering beamline at Elettra. *J. Synchrotron Rad.* **5**, 506–508 (1998).
55. Hammersley, A. P., Svensson, S. O., Hanfland, M., Fitch, A. N. & Hausermann, D. Two-dimensional detector software: from real detector to idealised image or two-theta scan. *High. Press. Res.* **14**, 235–248 (1996).
56. Blessing, R. H. An empirical correction for absorption anisotropy. *Acta Cryst. A* **51**, 33–38 (1995).
57. Sheldrick, G. M. A short history of SHELX. *Acta Cryst. A* **64**, 112–122 (2008).
58. Spek, A. L. Single-crystal structure validation with the program PLATON. *J. Appl Cryst.* **36**, 7–13 (2003).
59. Spek, A. L. PLATON SQUEEZE: a tool for the calculation of the disordered solvent contribution to the calculated structure factors. *Acta Cryst. C.* **71**, 9–18 (2015).
60. Nečas, D. & Klapetek, P. Gwyddion: an open-source software for SPM data analysis. *Open Phys.* **10**, 181–188 (2011).
61. Horcas, I. et al. WSXM: A software for scanning probe microscopy and a tool for nanotechnology. *Rev. Sci. Instrum.* **78**, 013705 (2007).
62. Tu, M., Wannapaiboon, S., Khaletskaya, K. & Fischer, R. A. Engineering zeolitic imidazolate framework (ZIF) thin film devices for selective detection of volatile organic compounds. *Adv. Funct. Mater.* **25**, 4470–4479 (2015).
63. Le Ouay, B. et al. Nanostructuration of PEDOT in porous coordination polymers for tunable porosity and conductivity. *J. Am. Chem. Soc.* **138**, 10088–10091 (2016).
64. Herzinger, C. M., Johs, B., McGahan, W. A., Woollam, J. A. & Paulson, W. Ellipsometric determination of optical constants for silicon and thermally grown silicon dioxide via a multi-sample, multi-wavelength, multi-angle investigation. *J. Appl. Phys.* **83**, 3323–3336 (1998).
65. Eslava, S. et al. Characterization of a molecular sieve coating using ellipsometric porosimetry. *Langmuir* **23**, 12811–12816 (2007).
66. Grzybowski, B. A., Qin, D. & Whitesides, G. M. Beam redirection and frequency filtering with transparent elastomeric diffractive elements. *Appl. Opt.* **38**, 2997–3002 (1999).
67. Tanuma, S., Powell, C. J. & Penn, D. R. Calculation of electron inelastic mean free paths (IMFPs) VII. Reliability of the TPP-2M IMFP predictive equation. *Surf. Interface Anal.* **35**, 268–275 (2003).

Acknowledgements

M.T. acknowledges the financial support from a Marie Skłodowska-Curie Individual Fellowship (no. 708439, VAPOMOF). R.A. acknowledges funding from the European Research Council (no. 716472, VAPORE) and the Research Foundation Flanders (FWO) for funding in the research projects G083016N and 1501618N and the infrastructure project G0H0716N. P.F. acknowledges funding from the European Research Council (no. 771834, POPCRYSTAL) and LP-03. J.T. and S.D.F. acknowledge support by FWO and KU Leuven internal funds. M.L.T. acknowledges the financial support from an FWO senior postdoctoral fellowship (12ZK720N). D.E.K. acknowledges the Marie Skłodowska-Curie Training Network (no. 765378, HYCOAT) for the financial support. This work was additionally supported (Z.W. and R.A.F.) by the DFG Priority Program 1982 COORNETs (www.coornets.tum.de). This research project has received funding from the EU's H2020 framework programme for research and innovation under grant agreements 801464 FETOPEN-1-2016-2017 and 654360 NFFA-Europe (proposal IDs 399, 462, 589, 596 and 854). T. Stassin and J. Marreiros are acknowledged for the help and discussions regarding the SAXS measurements. We thank E. Hedlund and M. Roeffaers for the assistance with the installation of the diffraction grating sensor setup, B. Raes and J. van de Vondel for the help with the EBL tool and M. Krishtab for the discussion on MOFs for low-*k* dielectrics.

Author contributions

M.T. and R.A. conceived and designed the experiments. M.T. carried out and analysed film deposition, patterning and characterization experiments. M.T., B.X., D.E.K., M.J.V.H., A.T. and P.F. carried out bulk MOF synthesis and characterization. M.T., B.X., D.E.K., I.S. and B.M. carried out the XRL patterning. M.T., B.X., D.E.K. and H.A. carried out SAXS measurements. A.J.C and T.H. conducted the XPS measurements. M.T., J.T. and S.D.F contributed to the AFM measurements. M.T. and M.L.T. designed and conducted the diffraction grating sensing. Z.W. and R.A.F. conducted QCM measurements. The manuscript was written by M.T. and R.A., with the input of all authors.

Competing interests

The authors declare no competing interests.

Additional information

Extended data is available for this paper at https://doi.org/10.1038/s41563-020-00827-x.

Supplementary information is available for this paper at https://doi.org/10.1038/s41563-020-00827-x.

Correspondence and requests for materials should be addressed to R.A.

Reprints and permissions information is available at www.nature.com/reprints.

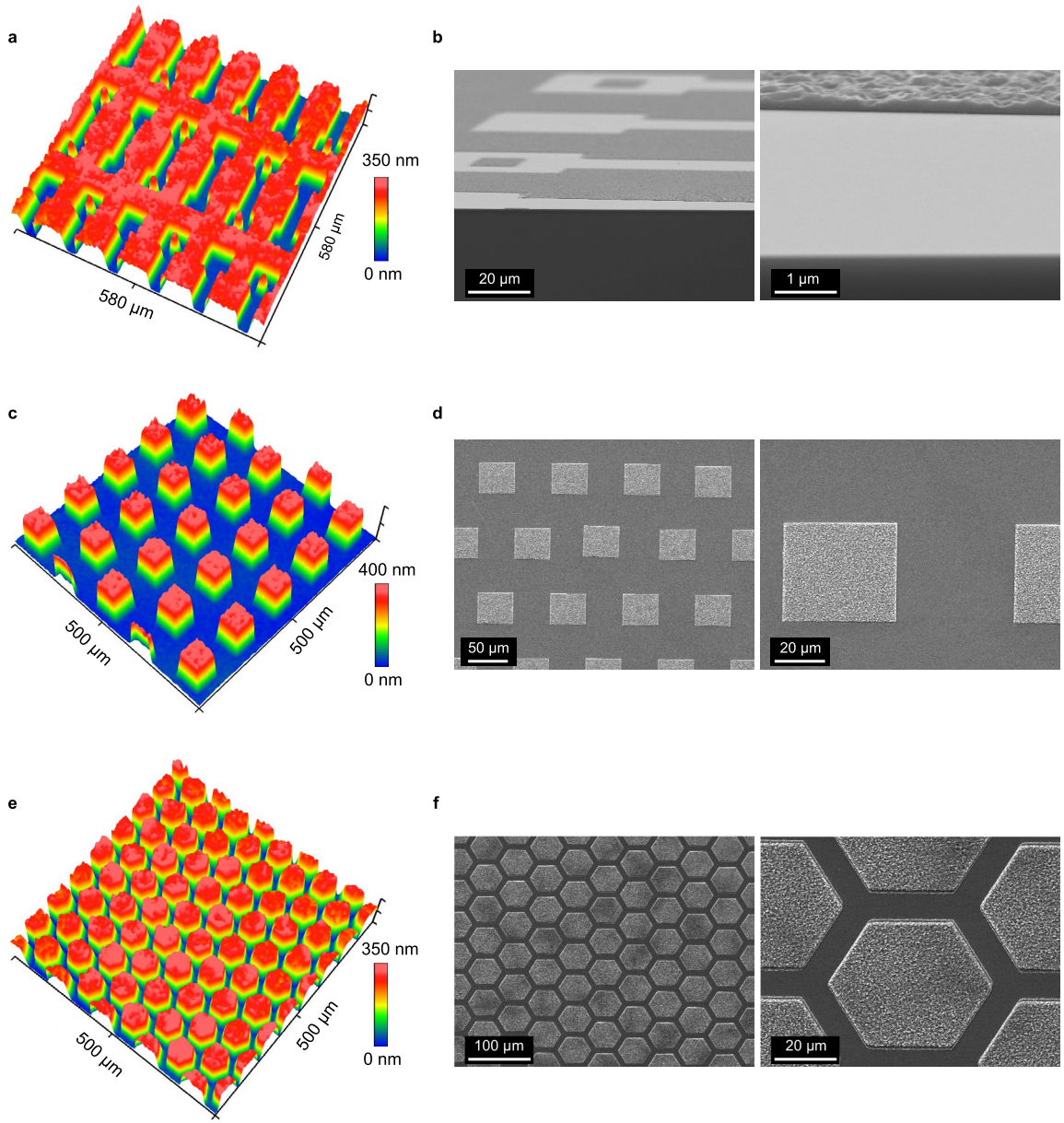

Extended Data Fig. 1 | XRL-patterned 300 nm thick ZIF-71 films. a, 3D optical profilometry of a ZIF-71 pattern (dumbbell shape), and the corresponding cross-section SEM images (**b**). **c**, 3D optical profilometry of a ZIF-71 patterns (square) and the corresponding top-view SEM images (**d**). **e**, 3D optical profilometry of a ZIF-71 patterns (hexagon) and the corresponding top-view SEM images (**f**).

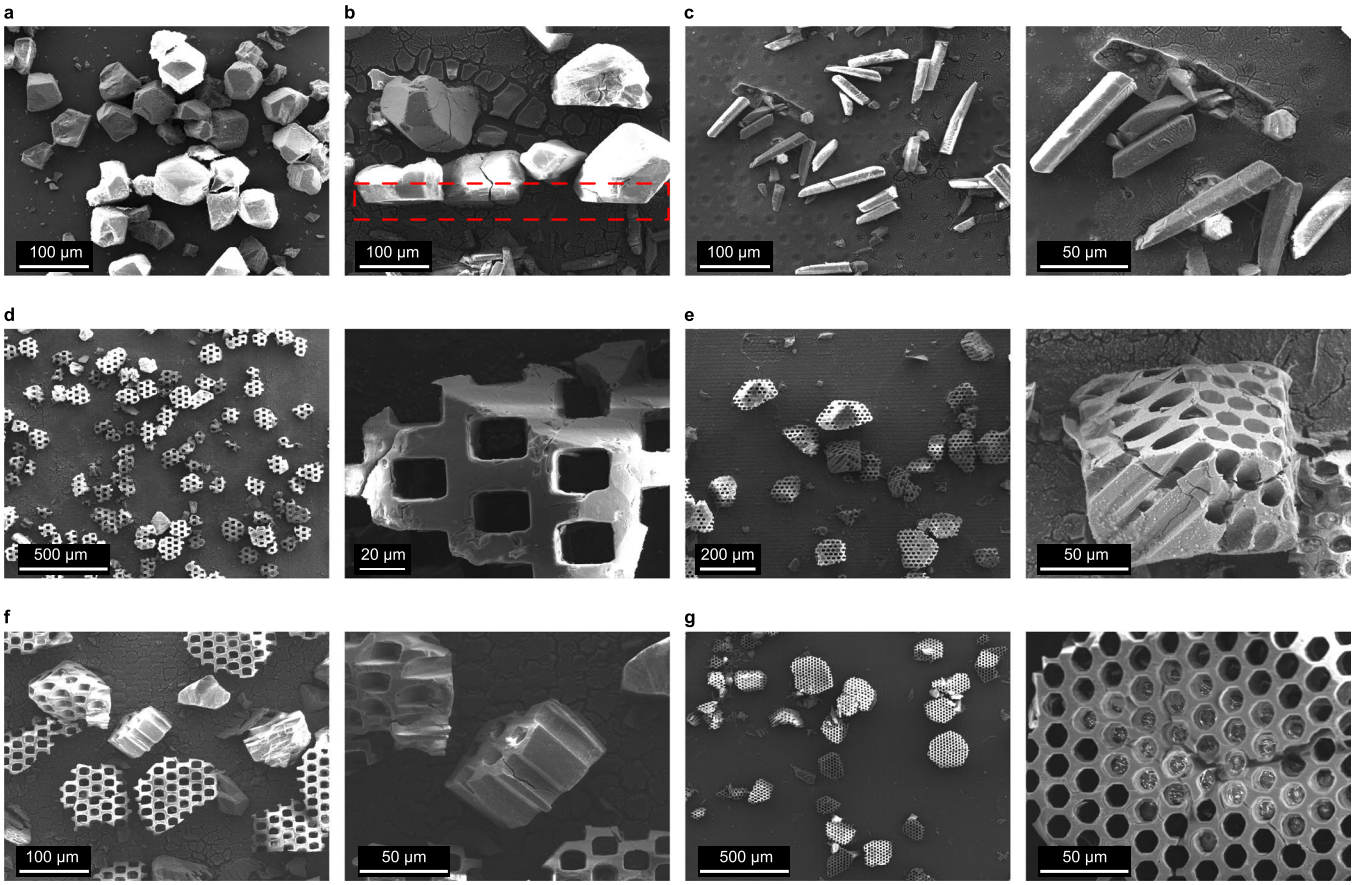

Extended Data Fig. 2 | XRL-patterned ZIF-8_Cl single crystals. a, SEM image of pristine ZIF-8_dcIm single crystals. **b**, SEM image of ZIF-8_dcIm single crystals of which part has been cut away via XRL (red dashed box). **c**, SEM images of ZIF-8_dcIm single crystals after XRL patterning with a negative hexagonal grid mask. **d-g**, SEM images of ZIF-8_dcIm single crystals after XRL patterning with different shaped positive masks. All crystals were spread on double-sided Kapton tape on a Si wafer. Because of the weak adhesion between the crystals and the substrate, some patterned crystals were tilted or fell over (*for example*, the rod-shaped crystals in panel **c**) after development. The imprint on the substrate occurs because of the X-ray-induced damage of the Kapton tape.

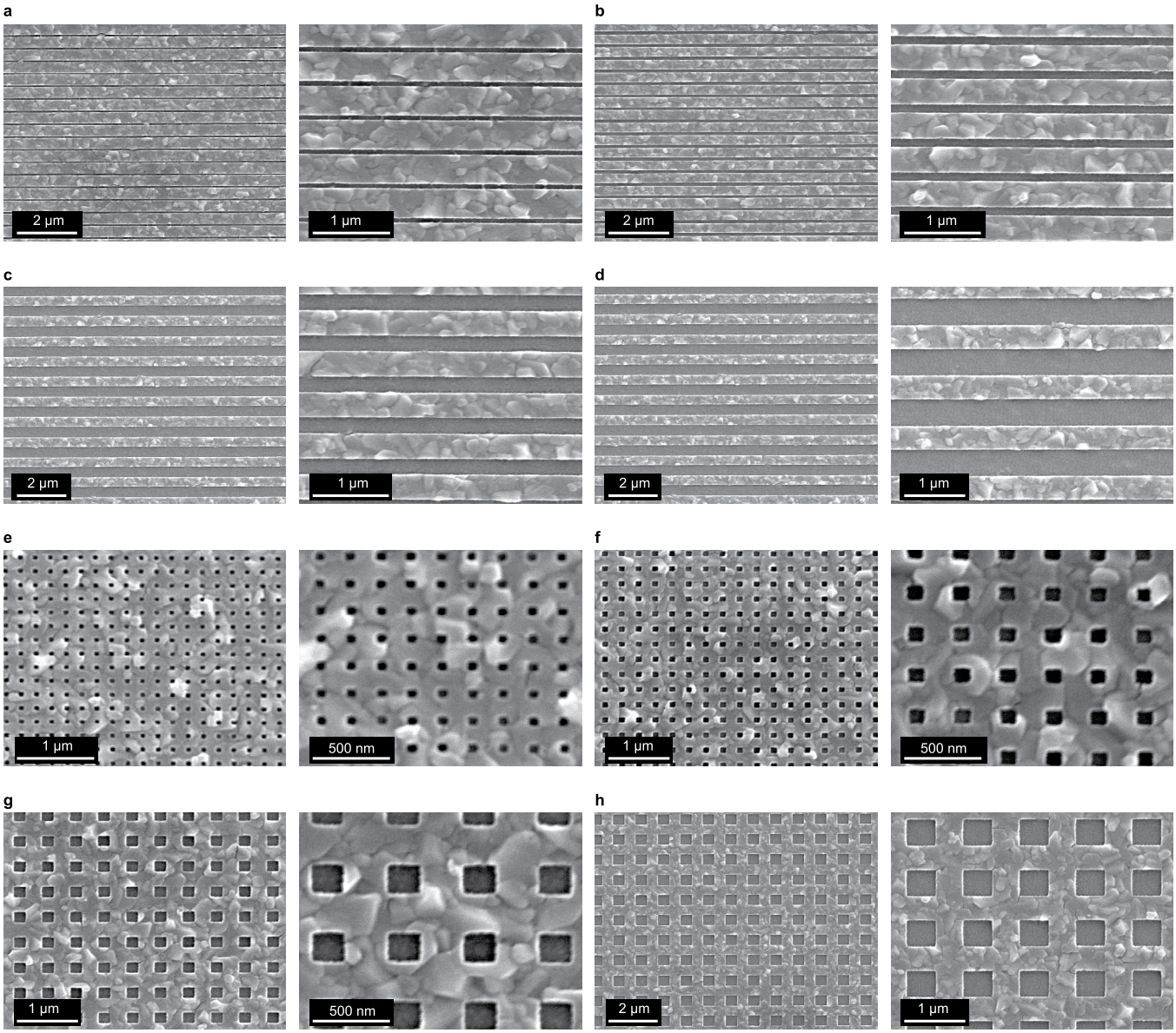

Extended Data Fig. 3 | EBL-patterned 100 nm thick ZIF-71 film. SEM images of EBL-patterned ZIF-71 patterns with different sizes of trenches: **a**, 70 nm; **b**, 100 nm; **c**, 200 nm; **d**, 500 nm. SEM images of EBL-patterned ZIF-71 patterns with different sizes of square-shaped holes: **e**, 70 nm; **f**, 100 nm; **g**, 200 nm; **h**, 500 nm.